

1 **Three-Dimensional Basin Depth Map of the Northern Los Angeles Basins from Gravity and**
2 **Seismic Measurements**

3

4 **Valeria Villa¹, Yida Li¹, Robert W. Clayton¹, and Patricia Persaud²**

5 ¹California Institute of Technology, Pasadena, CA, 91125.

6 ²Louisiana State University, Baton Rouge, LA, 70803.

7

8 Corresponding author: Valeria Villa (yvilla@caltech.edu)

9 **Key Points:**

- 10
- 11 • Passive seismic and gravity measurements are combined to estimate the 3D depth of the sediment-basement interface.
 - 12 • The maximum depth in the San Gabriel basin is 4.5 km, and Chino and San Bernardino
13 basins are less than 2 km deep.
 - 14 • The trace of the Raymond fault is delineated in the gravity anomaly of the San Gabriel
15 basin.

16 **Abstract**

17 The San Gabriel, Chino, and San Bernardino sedimentary basins in Southern California amplify
18 earthquake ground motions and prolong the duration of shaking due to the basins' shape and low
19 seismic velocities. In the event of a major earthquake rupture along the southern segment of the
20 San Andreas fault, their connection and physical proximity to Los Angeles can produce a
21 waveguide effect and amplify strong ground motions. Improved estimates of the shape and depth
22 of the sediment-basement interface are needed for more accurate ground-shaking models.

23 We obtain a three-dimensional basement map of the basins by integrating gravity and seismic
24 measurements. The travel time of the sediment-basement P-to-s conversion, and the Bouguer
25 gravity along 10 seismic lines, are combined to produce a linear relationship that is used to extend
26 the 2D profiles to a 3D basin map. Basement depth is calculated using the predicted travel time
27 constrained by gravity with an S-wave velocity model of the area. The model is further constrained
28 by the basement depths from 17 boreholes.

29 The basement map shows the south-central part of the San Gabriel basin is the deepest part and
30 a significant gravity signature is associated with our interpretation of the Raymond fault. The
31 Chino basin's western side is deeper relative to the eastern side. The San Bernardino basin,
32 bounded by the San Jacinto fault (SJF) and San Andreas fault zone, deepens along the edge of
33 the SJF. In addition, we demonstrate the benefit of using gravity data to aid in the interpretation
34 of the sediment-basement interface in receiver functions.

35

36 **Plain Language Summary**

37 The shaking levels in the metropolitan area of Los Angeles (LA) due to an earthquake on the San
38 Andreas fault are underestimated. Northeast of LA, the San Gabriel, Chino, and San Bernardino
39 basins influence the amount of shaking the LA area will experience. Sedimentary basins like these
40 can amplify and trap seismic waves. Understanding these basins' shapes will improve our velocity
41 model of the area and therefore seismic hazard estimates. The Basin Amplification Seismic
42 Investigation (BASIN) project deployed several seismic instruments across these basins to
43 characterize subsurface structures. Along with gravity measurements, which capture information
44 about the rock's density variations, we determine the basin depth and shape. The depth model is
45 then combined with the velocity model of the area to produce an improved model. Future shaking
46 models should take these improved models into account.

47 **1.1 Introduction**

48 In the event of a large earthquake rupture, sedimentary basins in the greater Los Angeles
49 area pose a significant seismic hazard. The Los Angeles Basin (LAB) is situated underneath the
50 mega-city of Los Angeles, a metropolitan city with a growing population. Extensive oil and gas
51 exploration in the area provided a rich data set of the subsurface for detailed basin mapping
52 purposes. Northeast of the LAB is the San Gabriel, Chino, and San Bernardino basins. The shape
53 and depth of these basins are not well constrained because of the lack of seismic surveys in the
54 area, particularly active source surveys used for oil and gas exploration. During a large
55 earthquake rupture, the basins trap and amplify seismic waves which highly depend on the
56 thickness, geometry, and material properties of the sedimentary layers within the basin (Frankel,
57 1993). A wave-guide effect between these northern basins and the LAB is hypothesized. The
58 hypothesized waveguide effect channels the amplified energy towards downtown Los Angeles for
59 events on the southern San Andreas fault (Olsen et al., 2006). Current ground-shaking models in

60 the greater Los Angeles area appear to underestimate the level of ground shaking for earthquakes
61 on the southern segment of the San Andreas fault by a factor of 4 (Denolle et al., 2014). Accurate
62 knowledge of the basin shape and edges will help resolve localized amplification and interference
63 effects (Magistrale et al., 2000).

64 The primary goal of the Basin Amplification Seismic INvestigation (BASIN) project is to
65 improve the 3D seismic velocity model and structural knowledge of the basins in the northern Los
66 Angeles area. This improved model will help to provide a better estimate of the ground shaking.
67 Here, we integrate results from the BASIN receiver function profiles (Liu et al., 2018; Wang et al.,
68 2021; Ghose et al., 2022) with gravity data and use a 3D seismic velocity (V_s) model obtained
69 from the BASIN dataset (Li et al., 2022) to map the basement depth of the San Gabriel, Chino,
70 and San Bernardino basins. Previous geophysical studies, borehole data, groundwater
71 management reports, and geologic maps are used as additional constraints on the final model.
72 The advantage of this approach is that it allows us to extend the detailed sediment-basement
73 depths from our dense nodal survey to 3D to produce the first integrated basin model for the
74 region.

75

76 1.2 Geologic Setting

77 The San Gabriel basin is a triangular-shaped sedimentary basin bounded by the San
78 Gabriel Mountains on the north, San Jose and Puente Hills on the east, and Repetto and
79 Montebello Hills on the west (Yeats, 2004, Figure 1). The Pliocene-Pleistocene sedimentary fill is
80 comprised of a basal shallow-marine sequence overlain by the non-marine Duarte Conglomerate
81 and underlain by a basement boundary composed of the Peninsular Ranges batholithic and
82 metamorphic rocks such as gneiss (Fuis et al., 2001; Yeats, 2004; Brocher, 2005). Major faults
83 bound the sedimentary fill of the basin with the Sierra Madre fault on the north and Puente Hills
84 blind-thrust in the south (Figure 1b). The west side is marked by the northwest-striking, right-slip
85 East-Montebello fault; and the east side by the northeast-striking, left-slip Walnut Creek fault and
86 Indian Hill fault (Figure 1b). The northeast-striking segment of the Raymond fault separates the
87 deeper San Gabriel basin from the shallower Raymond basin. Wright (1991), Brocher, (2005),
88 and Fuis et al. (2001) estimated the maximum depth of the San Gabriel basin as 3, 3.7, and 5
89 kilometers (km), respectively. Yeats (2004) inferred the basin trends with a southwest depression
90 towards the Montebello and Repetto Hills and an upward plunge towards the Raymond fault.

91 The Chino basin is one of the largest groundwater basins in Southern California and the
92 largest in the upper Santa Ana Valley. It is bounded by the Puente Hills on the west, the Jurupa
93 Hills on the southeast, and the San Gabriel Mountains on the north (Figure 1a). The basin is fault
94 bounded by the northeast-striking San Jose fault, northeast-striking Cucamonga fault, southeast-
95 striking Chino fault, and northwestern-striking Rialto-Colton fault (Figure 1b). Tectonic forces
96 uplifted neighboring mountains and depressed the basin along major fault zones (Wildermuth et
97 al., 2005). The depth of groundwater in the northernmost and southernmost parts is less than 152
98 meters and 4.50 m, respectively, and groundwater movement is north to south (Blomquist, 2021;
99 Dutcher & Garrett, 1963). The bedrock is comprised of a mix of metamorphic, igneous, and
100 consolidated sedimentary rocks.

101 The San Bernardino basin is a wedge-shaped sedimentary basin bounded by two major
102 fault zones: the San Jacinto Fault zone (SJFZ) to the west and the San Andreas Fault zone
103 (SAFZ) to the east (Figure 1). The San Gabriel and San Bernardino Mountains border the northern
104 and eastern sides of the basin, and on the southern side are the Crafton Hills and Jurupa Hills.
105 The basin's deepest part resembles a pull-apart structure from the Quaternary extension of the

106 major right-step faults of the San Jacinto and San Andreas fault zones (Anderson et al., 2004;
107 Morton & Miller, 2006). The filling of unconsolidated Quaternary and Tertiary alluvial-fan deposits
108 cover the consolidated, non-water bearing Tertiary deposits (Dutcher & Garrett, 1963; Frankel,
109 1993). The sedimentary section overlies the pre-Tertiary igneous and metamorphic basement
110 rocks (Dutcher & Garrett, 1963). The basement rock types are composed of Peninsular Ranges-
111 type (i.e. granodiorite, quartz diorite, tonalite, and gabbro), San Gabriel Mountains-type (Pelona
112 Schist, and prebatholithic crystalline rocks intruded by Mesozoic plutons), Southeastern San Gabriel
113 Complex (i.e. granitic rocks, migmatite, and gneiss), and San Bernardino Mountain-type
114 (Anderson et al., 2004). There are a few basement depths documented from water and oil wells,
115 and records mostly cover the northeastern edges of the basin with a maximum basement depth
116 of around 1.2 km (Dutcher & Garrett, 1963). Stephenson (2002) studied 14 km of seismic
117 reflection data through the San Bernardino area and inferred a depth of 1.7 km near the San
118 Jacinto fault. Anderson et al. (2004) combined gravity and aeromagnetic data to map the San
119 Bernardino basin and found that the largest amount of extension is along the San Jacinto fault
120 with a maximum depth of 2 km. Catchings et al. (2008) found a shallower basin depth (closer to
121 1.2 km) based on two seismic profiles in the San Bernardino basin.

122 **2 Materials and Methods**

123 **2.1 BASIN Project and Receiver Functions**

124 This study integrates seismic and gravity measurements to determine the shape and
125 depth of the San Gabriel, Chino, and San Bernardino basins. The BASIN project deployed
126 approximately 744 seismic nodes from 2017 to 2019, with an average 250-m spacing, across ten
127 seismic lines (Figure 1). The prefix SG is used for lines in the San Gabriel basin and SB for lines
128 in the Chino or San Bernardino basin. Seismic line SB1 crosses all three northern basins and is
129 the longest line. The San Gabriel basin has four lines: SG2, SG1, SG3, and SG4; the Chino basin
130 has three lines: SB4, SB3, and SB5; and the San Bernardino basin has two lines: SB2, SB6, with
131 the basins and lines listed from west to east. The dense intra-line spacing provides the spatial
132 detail used to constrain the basement shape.

133 Receiver functions (RFs) were computed along the 10 seismic lines by three principal
134 studies within the BASIN project (Liu et al., 2018; Wang et al., 2021; Ghose et al., 2022). These
135 studies concentrated on acquiring the basement-sediment interface, other intra-crustal layers,
136 and the Moho discontinuity, as well as characterizing possible fault offsets. Travel times
137 associated with the sediment-basement interface were determined from the P-S converted
138 phases in the RFs. Liu et al. (2018) applied traditional frequency domain deconvolution to
139 teleseismic events from a 35-day nodal set along SG1, SG2, and SB4 and showed the Moho
140 discontinuity, basement bottom, intermediary sedimentary layers, and offsets along with the Red
141 Hill and Raymond faults. Wang et al. (2021) used a Bayesian array-based coherent receiver
142 function method and multiple events at each station to constrain basin geometry by leveraging
143 the close station-spacing of these short-term dense arrays to aid in suppressing the noise and
144 non-uniqueness of the deconvolution process. The study showed promising lateral layers in the
145 subsurface structure. Ghose et al. (2022) applied a traditional frequency domain deconvolution
146 receiver function method to the nodal dataset, interpreted single-event RF profiles, and showed
147 complex, non-uniform basement topography, evidence of an intra-crustal interface, and a well-

148 defined Moho discontinuity. Detailed information about the BASIN nodal deployment and receiver
149 function work can be found in Clayton et al. (2019) and the respective studies mentioned above.

150 While these RF studies imaged the sediment-basement interface, there are subtle lateral
151 differences among the studies likely due to noise and rapid lateral variations in the structure. The
152 use of gravity measurements along the lines helps distinguish the sediment-basement interface.
153 In this study, the final time-to-basement is determined from all three RF studies.

154 **2.2 Residual Bouguer Gravity**

155 We extracted Bouguer gravity station data for the northern basins from the Pan-America
156 Center for Earth and Environmental Sciences gravity portal which included four independent
157 gravity measurements (PACES, 2012); Figure S1). The gravity data obtained from PACES (2012)
158 can be downloaded at <http://dx.doi.org/10.22002/D1.20256>. The Bouguer gravity points were
159 interpolated to a 100-m spacing grid using a nearest-neighbor inverse-distance weighting
160 interpolation scheme to create a Bouguer gravity map of the BASIN study area (Figure 2a). We
161 removed the regional trend from the gravity dataset to isolate the individual basin effects. Geologic
162 knowledge of the area offers insight into how to properly estimate the regional trend. Since the
163 northern basins have different evolutionary histories and distinct strong, nearby gravity signature
164 sources like the Los Angeles basin, we separated the residual calculation for the San Gabriel
165 basin from the Chino and San Bernardino basins. We used information gathered from the geologic
166 map that highlights areas of exposed bedrock (Figure 1a), trends from the RF profiles, and
167 borehole depths (Table S1). The regional trend of the San Gabriel basin was fitted with a second-
168 order polynomial trend that included the San Gabriel Mountains to the north, Repetto Mountains
169 to the south, East Montebello Mountain to the southwest, and Eagle Rock hills to the west while
170 excluding the Los Angeles basin (Figure 1a and 2b). The San Bernardino and Chino residual
171 calculation was computed by fitting a seventh order polynomial over the San Jose Hills to the
172 west, the eastern section of San Gabriel Mountains to the north, San Bernardino Mountains to
173 the east, and Jurupa Hills to the south (Figure 1a and 2c). The regional trend was subtracted from
174 the Bouguer gravity to obtain the residual Bouguer gravity (Figure 2a, 2d).

175 Residual Bouguer gravity highlights the effect of subsurface density variations, including
176 those due to the topography of the sediment-basement interface. There are different approaches
177 to using residual Bouguer gravity to estimate crustal structure and the depth of sedimentary
178 basins, especially when paired with another geophysical measurement. Tondi et al. (2019)
179 employed a joint inversion of passive seismic and Bouguer gravity data to recover a 3D density
180 model of Northern Italy. Florio (2020) used a depth-gravity relationship where known control

181 points of basement rock depth are related to the residual Bouguer gravity to estimate the thickness
 182 of the Yucca flat basin, Nevada.

183 **2.3 Integration of Seismic and Gravity Measurements**

184 We use Bouguer's formula for a basin embedded in a block of thickness H of density ρ_1 ,
 185 and basin of thickness h with density ρ_2 , given as

$$186 \quad \delta g = 2\pi G(\rho_1)H + 2\pi G(\rho_2 - \rho_1)h \quad (1)$$

187 to linearly relate the gravity anomaly to density and thickness. This establishes a simple linear
 188 relationship between the residual Bouguer gravity, δg , and the travel time of the converted phase
 189 from the sediment-basement interface, t ,

$$190 \quad \delta g = a + bt \quad (2)$$

191 where a and b are parameters to be determined by fitting δg to t . Expressing equation (1) in the
 192 form of equation (2) allows us to relate the residual gravity to the time-to-basement across the
 193 basins. Parameter a represents the Bouguer gravity of a block of thickness H with density ρ_1 .
 194 Parameter b scales t so that it represents the contributions of a basin of thickness h and density
 195 ρ_2 relative to the embedded block. We calculate the parameters using equation (2) with observed
 196 Bouguer gravity values and time-to-basement using a least-squares method for each of the ten
 197 seismic lines. Since we have gravity values in a three-dimensional mesh, we interpolated the a
 198 and b parameters from the lines to the three-dimensional mesh using an inverse-distance
 199 weighted interpolation scheme. We were then able to predict the time-to-basement away from the
 200 lines, constrained by the residual gravity anomaly values using the inverted equation (2), $t =$
 201 $(\delta g - a)/b$, thus extending from a two-dimensional model to a three-dimensional one.

202 **2.4 Iterative Basement Depth Computation with Shear Wave Velocity Model**

203 Depth to the basement was calculated using the predicted time obtained from equation 2
 204 and a shear wave velocity model (Li et al., 2022). The depth was estimated by assuming vertical
 205 incidence for a given Ps or PpPs phase. The Ps phase formula is given by

$$206 \quad t_{Ps} - t_P = \int_0^h \left(\frac{1}{\beta} - \frac{1}{\alpha} \right) dz \quad (3)$$

207 and for the PpPs phase by

$$208 \quad t_{PpPs} - t_P = \int_0^h \left(\frac{1}{\beta} + \frac{1}{\alpha} \right) dz \quad (4)$$

209 where z is depth, h is the basin depth, V_s is the S-wave velocity, V_p is the P-wave velocity, t_P is
 210 the direct P-arrival time, t_{Ps} the Ps arrival time, and t_{PpPs} is the PpPs arrival time based on the
 211 receiver function profiles. S-wave velocities were obtained using an ambient noise cross-
 212 correlation approach (Li et al., 2022). S-wave velocities were converted to P-wave velocities using

213 an empirical formula (Brocher, 2005) valid for S-wave velocities between 0 and 4.5 km/s excluding
 214 calcium-rich, mafic, gabbros, and serpentine rocks:

$$215 \quad V_p(\text{km/s}) = 0.9409 + 2.0947V_s - 0.8206V_s^2 + 0.2683\beta V_s^3 - 0.0251V_s^4 \quad (5)$$

216 An initial depth model was calculated using the equation

$$217 \quad h = \beta t_{Ps} \frac{K}{K-1} \quad (6)$$

218 where K is the V_p/V_s ratio. Equation (6) was derived from (3) and assumes a Ps phase recorded
 219 at sea level. We averaged the S-wave velocities across 1 km of the sedimentary column from the
 220 initial S-wave velocity model to compute K for each point in the mesh. Initial P-wave velocities
 221 were computed using equation (5).

222 Li et al. (2022) then used the initial depth model as a prior for the shear wave velocity
 223 inversion. The inversion of the Vs model is highly dependent on the initial model that uses the
 224 basin depth as a constraint. Using the shear wave velocity results, the depth was recalculated
 225 using equations (3) or (4) depending on which converted phase is used. A linear relationship
 226 between the modeled depth and the predicted time-to-basement was established to fill in for the
 227 few points in the mesh that did not converge. We used an iterative process instead of solving an
 228 inverse problem because of the nonlinearity of the method. The prior basin model was provided
 229 for the Vs inversion and the new Vs model for the depth model calculations.

230 The algorithm outputs the estimated basement depth when the difference between S-
 231 wave travel time and P-wave travel time (3) or when the sum of S and P wave travel time (4)
 232 approximately equaled the sediment-basement interface time based on the RF studies. For the
 233 San Gabriel basin, we assumed a primary phase, Ps, while for the Chino and San Bernardino
 234 basins a PpPs phase. Our justification for using a PpPs phase was based on the shallower
 235 sedimentary basin (< 2 km) obtained with equation (4) that agrees well with other independent
 236 sources. For instance, two boreholes in the Chino basin support a basin shallower than 2 km. The
 237 Chino Basin Management report by Wildermuth et al. (2005) showed multiple (>50) boreholes
 238 that penetrated sedimentary and crystalline basements at shallow depths (< 2 km; see Wildermuth
 239 et al. (2005) report for exact boreholes locations). Two boreholes not associated with groundwater
 240 monitoring showed depths less than 1 km (Table S1). In addition, multiple studies in the San
 241 Bernardino basin indicate measured depths of less than 2 km as mentioned in Section 1.2.

242 **2.5 Integration of Borehole Basement Depths**

243 Multiple borehole logs with recorded basement depth allowed us to constrain and
 244 corroborate our final depth model. There is a total of 17 borehole logs with recorded basement
 245 depths: 11 in the San Gabriel basin, 2 in the Chino basin, and 4 in the Raymond basin (Table S1).
 246 Because the Chino basin contains only two borehole measurements, we assessed the model
 247 based on the closeness to the recorded depth and shifted all points in the Chino and SB basin
 248 mesh 500 m down to match the boreholes and previous maximum depths found in studies
 249 mentioned in Section 1.2. Borehole measurements provided another advantage in areas of poor
 250 interpolation of the inversion parameters. Such is the case in the Raymond basin where the
 251 interpolated parameters from equation (2) are influenced by the gravity response and time-to-
 252 basement of SG2. It is difficult to evaluate this basin based on the response of SG2 because this
 253 line crosses the deeper SG basin and the edge of the Raymond basin. Thus, the depths in this

254 area were estimated using this quadratic depth-gravity relation using 4 control borehole points
255 (Table S1) obtained from the Buwalda (1940) report.

256 **3 Results**

257 **3.1 Time-to-Basement and Residual Bouguer Gravity Profiles**

258 Figures 3 to 4 show the final basement interpretations for SG2 and SG1 and the results
259 from two RF studies. Results for SG3 and SG4 are shown in Figure S2. All four lines show a good
260 linear relationship between the time-to-basement and the residual Bouguer gravity. The sediment-
261 basement boundary interpretation along lines SG2 and SG4 were modified based on the
262 geological interpretations of the gravity signatures and/or other factors which will be discussed
263 later. Lines SG1 and SG3 followed Wang et al. (2022) interpretation of the sediment-basement
264 interface. The part of SB1 in the San Gabriel basin was reinterpreted based on Wang et al. (2021)
265 and Ghose et al. (2022). The SG2 line crosses the intersection of the Eagle Rock fault and the
266 Raymond fault (Figure 3). The change in topography associated with the fault scarp is evident in
267 the gravity profile of SG2 which shows a steep gradient dipping to the south (Figure 3b). The East
268 Montebello fault runs near parallel to SG2 and merges the Raymond fault. The SB1 line intersects
269 the East Montebello fault, and a significant gravity gradient is also present near the steep gradient
270 found along SG2.

271 All sediment-basement interfaces in the Chino basin were reinterpreted following Wang et
272 al. (2021), Ghose et al. (2022), and gravity trends. Figure 5 shows the SB4 profile with large
273 negative residual Bouguer gravity values and longer basement-time to the north. The SB3 and
274 SB5 lines are shown in figures S3 and S4. The SB3 profile shows the opposite trend with lower
275 gravity values and larger times to the south relative to the north. The gravity lows between each
276 north and south section of the lines are lower in the SB4 line than in the SB3. The SB5 profile
277 depicts a similar trend to that observed along SB4, with negative values concentrated to the north,
278 abutting the San Gabriel Mountains. In contrast to the SB4 and SB3 lines, the SB5 line shows a
279 negative value that curves upwards to positive values and then gradually decreases to the south.
280 The depression in the south has higher gravity values than those in the north.

281 The San Bernardino basin lines (SB2 and SB6) have a good correlation between negative
282 gravity values and longer travel time-to-basement along the San Jacinto Fault (SJF) (Figure 6
283 and S5). The SB2 profile follows Wang et al. (2021) version of the sediment-basement interface
284 and SB6 follows Ghose et al. (2022) values. It should be noted that Ghose et al. (2022) picks on
285 SB2 agreed with the Wang et al. (2021) values except for the northern section. The southern
286 section of SB2 shows the lowest gravity values in the basin and the time reflects this trend. The
287 SB6 line also reflects this trend based on the lower negative values to the east of the line, which
288 ends near the SB2 line.

289 **3.2 3-D Residual Bouguer Gravity Model**

290 The residual Bouguer gravity for the San Gabriel basin shows prominent gravity signatures
291 over faults, mountains, and basins. A steep gravity gradient extends 10 km from Repetto Hills
292 toward the Sierra Madre fault, which aligns well with the mapped Raymond fault trace (Figure 1b).
293 A smaller triangular block extending northwest of the intersection of the Eagle Rock fault and the
294 Raymond fault shows the highest gravity values in the San Gabriel basin and is assumed to be
295 caused by the Repetto Hills and associated exposed conglomerate and sandstone of the Topanga

296 Group (Yerkes & Campbell, 2005, Figure 1b). Another gravity gradient trending northwest strikes
297 subparallel to the East Montebello fault. The northern central part of the San Gabriel basin shows
298 high gravity values that extend eastward towards SG4. The southern central part shows the
299 lowest gravity values in the basin. Gravity highs increase steadily from the central lows towards
300 SG3 between the San Jose Hills and the San Gabriel Mountains (SG4), which is marked by a
301 channel-like feature in the gravity anomaly.

302 Gravity highs are encountered in the east and lows in the west of the Chino basin. The
303 location of SB3 represents a close approximation of this division in gravity values (Figure 1b). The
304 highest positive values are in the southeast and are likely due to the exposed basement in the
305 Jurupa Hills composed of quartz-biotite gneiss, impure quartzite, biotite-quartz schist, marble,
306 calc-silicate contact rocks, and amphibole schist (MacKevett, 1950, Figure 1a), that produce a
307 positive density contrast against the low-density basin fill. In the southern segment of SB3, there
308 are negative values surrounded by positive values. The Jurupa Valley is approximately located
309 near these negative values. These lower density sediments from the Jurupa Valley are contrasted
310 against the exposed Jurupa Hills rocks to the northeast-east and older alluvium-fan deposits to
311 the west. A strong gravity gradient signature divides the Chino basin and San Bernardino basins.
312 This strong gravity gradient correlates well with the SJFZ, a series of right-lateral strike-slip faults
313 (Figure 1b).

314 The lowest gravity values associated with the San Bernardino basin are along the SJF.
315 The gravity values then increase towards the root of the San Bernardino Mountain and the SAF.
316 The higher gravity values are due to the metamorphic basement rock composition of the San
317 Bernardino Mountains. The low values are associated with the basin fill comprised of
318 unconsolidated Quaternary and Tertiary alluvial-fan deposits overlying the consolidated, non-
319 water bearing Tertiary deposits. The lower gravity values in the northern part of the San
320 Bernardino basin might be explained by the southeastern San Gabriel Complex, likely from the
321 black belt of the magnetic mylonitic rocks (Anderson et al., 2004; Nourse, 2002).

322 **3.3 3D Basin Depth Map Model**

323 Figure 7 shows the final basement depth model for the northern Los Angeles basins. The
324 San Gabriel basin is triangular shaped and bounded by the Raymond fault to the northwest, the
325 Sierra Madre fault to the north, the San Jose fault to the east, and the East Montebello fault to the
326 west. The Raymond fault separates the Raymond basin from the San Gabriel basin and acts as
327 an impermeable barrier (Buwalda, 1940). The Raymond basin has depths up to 365 m. The
328 Raymond fault shows potential vertical offset with a change in basement depth of nearly 1 km
329 across the fault. The Sierra Madre fault shows three spatial barriers of varying depth based on
330 the basin depth map: one near the boundary of the Raymond basin, a central deeper segment
331 near borehole 7, and a shallower depth offset between SG3 and SG4. The San Jose fault is
332 mapped in an area of shallow basement depths. The East Montebello fault is in a region of uplift
333 in the north and subsidence in the south. Basement depths are shallow near the Eagle Rock and
334 Raymond fault intersection and decrease southeastwards towards Montebello, CA. At the
335 southern end of SG1, there is an uplift that might extend further south towards the Montebello
336 Hills. East of this uplift near SG3, the basin resumes depths of 3-4.5 km, which continue
337 throughout most of the basin.

338 The Chino basin is deeper east of SB4 and has shallower depths around the SB3 and
339 SB5 lines. The deeper areas are two regions with 2-2.5 km basement depth within an irregularly

340 shaped area of shallower basement (1-1.5 km depth). The SB3 line shows sedimentary layers
 341 with varying thicknesses. The SB3 is slightly deeper in the south relative to the north. The 3D map
 342 depicts this southward deepening trend merging to the 1-1.5 km deep irregular shape previously
 343 mentioned. Basement depths are much shallower along SB5 compared to SB3 and SB4. These
 344 shallower depths are likely due to the Jurupa Hills in the south (Figure 1b). Unlike the southern
 345 segment, the northern segment of SB5 is deeper and dips east northward.

346 Basement topography in the San Bernardino basin reveals a clear pattern of subsidence
 347 along the SJFZ. Figure 6 shows the SB2 depth profile deepening towards the south near the SJFZ
 348 and shallowing towards the SAF and the San Bernardino Mountains. Similarly, the basement
 349 along the SB6 profile deepens to the west towards the SB2 (Figure S5). The estimated basement
 350 depth map for the San Bernardino basin shows depths of ~2 km along the southern part of the
 351 SJFZ. The basement depths increase gradually to 1 km towards the San Bernardino Mountains
 352 and the SAF. There exists a separate deeper region with depths close to 2 km towards the north
 353 of the SJFZ. This area extends to the west of the Chino basin and is observed in the northern
 354 segment of the SB5 line as previously described.

355 **3.4 Basement Depths Uncertainty**

356 The uncertainty of the basement depths might be due to rocks within the basin with
 357 different densities, the misfit between the predicted and observed residual Bouguer gravity due
 358 to shorter wavelength geologic features not included in the model, or the uncertainties in the
 359 velocity model. While extensive work was done to remove the regional trend from the Bouguer
 360 gravity values to ensure they represent the basin fill, there were areas where we could not capture
 361 all local effects within the basin. Line SG4 shows this uncertainty and is discussed in Section 4.
 362 Furthermore, the Vs model has areas of low ray path coverage which might result in outliers
 363 affecting the depth calculation. The southern part of SB3 best illustrates this uncertainty and is
 364 discussed in Section 4. Another source of uncertainty is reflected in the predicted time-to-
 365 basement that may correspond to a negative RF phase instead of a positive phase like Ps or
 366 PpPs. A possible reason for this is the predicted time constrained by gravity comes with
 367 uncertainties such as those mentioned above but is also dependent on density contrasts and a
 368 and b parameters. In contrast, the RF conversions reflect impedance contrasts suggesting that
 369 there are instances where the two may not match. Nevertheless, the inversion for the time-to-
 370 basement is more sensitive to the b parameter than other inversion parameters.

371 **4 Discussion**

372 Here we discuss the interpretation of the sediment-basement interface based on the
 373 sources of the gravity anomalies and the time-to-basement and how these interpretations along
 374 with borehole data aided our final basement depth map for each basin. Table S1 summarizes
 375 the borehole data and drilled basement depths used to constrain the final basin model.

376 The San Gabriel basin reveals a triangular-shaped basement bounded by major strike
 377 slips and thrust faults. The most prominent gravity gradient in the San Gabriel basin aligns with
 378 the trace of the left-lateral strike-slip Raymond fault. The source of this gravity anomaly is likely
 379 due to the offset of basement ridges, which juxtaposes blocks with different basement elevations.
 380 Weaver and Dolan (2000) reported a 3.4 km left-lateral offset of a crystalline basement ridge at
 381 the east end of the Raymond fault. The Raymond fault separates the Raymond and the San
 382 Gabriel basins. While the Raymond basin is included in the model, there are insufficient nodal

383 stations located there aside from the northern part of SG2, to constrain the Raymond basin and
384 the residual Bouguer gravity might not capture the local effects of this shallower basin in
385 comparison to the larger and more prominent San Gabriel basin. The majority of our interpretation
386 of the Raymond basin comes from Buwalda (1940) where it was concluded that the Raymond
387 fault acts as an impermeable barrier between the shallower Raymond basin and the San Gabriel
388 basin. Estimated depths of the Raymond basin range from 250 to 1000 m.

389 Another gravity high within the San Gabriel basin study region is observed near Eagle
390 Rock, Raymond, and East Montebello faults intersection. Near the intersection, we observe a
391 steep gravity gradient signature along the SG2 and SB1 lines (Figure 2d, 3). The source of this
392 gravity high may be explained as a result of a restraining bend from the Raymond fault (Weaver
393 & Dolan, 2000). East of the intersection, the source is attributed to the displacement of old
394 crystalline rocks of the San Rafael Hills from the Tertiary rocks (Buwalda, 1940). Due to the
395 prominent gravity signatures that delineate the traces of faults, we reinterpreted the sediment-
396 basement interface in the time-to-basement profile to reflect this sharp steep gradient that is not
397 reflected in the RF profiles.

398 The third gravity high aligns with the East Montebello fault, which runs parallel to SG2.
399 While this fault bounds the southwest boundary of the San Gabriel basin and separates it from
400 the Los Angeles basin, the sedimentary layer thickness is not consistent along the strike of the
401 fault or the SG2 line. Basement depths closer to 2 km in its southern segment and 1 km to the
402 north suggest the East Montebello fault may not be a purely right-slip fault but may have a
403 component of non-uniform vertical separation along strike, allowing more accommodation space
404 to be created at its southern end. Yeats (2004) found the southwestern part of the East Montebello
405 fault was subsiding more than the northeast area. In addition to the East Montebello fault
406 interpretation, the positive residual gravity values also likely reflect the Repetto Hills which were
407 uplifted by the Elysian Park anticlinorium (Dolan et al., 2001).

408 The central segment of the San Gabriel basin depth map (Figure 7) is divided into two
409 deeper sedimentary sections by a central high near the middle of the SG1 line intersection.
410 Figures 4 and S3 show a uniform increase in sedimentary layer thickness towards the south,
411 suggesting a deeper southern basin. However, the southern end of SG1 also shows a slight
412 decrease in thickness, which is attributed to the Hacienda Hills. Along the southern rim of the San
413 Gabriel basin, the Repetto Hills are located to the west and the Hacienda and Puente Hills are
414 located on the central and east-central sides. The easternmost end of the basin, however, shows
415 a deepening along the left-lateral Walnut Creek fault. While the Walnut Creek fault shows no
416 tectonic geomorphic expression, it separates the flat-lying strata of the San Gabriel basin from
417 folded strata of the San Jose and Puente Hills (Yeats, 2004).

418 The connection between the San Gabriel and the Chino basins is best illustrated using
419 our interpretation of the SG4 line (Figure S2). Due to its proximity to both the San Gabriel and
420 Chino basin, this line provides insight into the edges of both basins. Evaluating the 3D basin depth
421 map around this region we find that this area acts more as a saddle with a decrease in depth from
422 the west to an increase in depth to the east and then a gradual decrease further east. The slope
423 in basement topography is more gradual towards the Chino basin and steeper towards the San
424 Gabriel basin. This is an important factor when determining the impact of the channeling
425 waveguide effect of a seismic event. However, there is large uncertainty in the sediment-

426 basement interpretation due to conflicting RF interface interpretations and residual gravity values
427 along the SG4 line.

428 The SG4 sediment-basement interface from the RF studies was reinterpreted due to
429 opposing gravity and RF slopes since slopes need to have the same sign for proper time-to-
430 basement inversion. The RF studies from Ghose et al. (2022) and Wang et al. (2021) show time-
431 to-basement increasing to the south, with Wang et al. (2021) having slightly larger values in the
432 south (Figure S2e). The gravity signature, however, showed the gravity decreasing northwards,
433 towards the base of the San Gabriel Mountains (Figure S2f). It is quite possible that the residual
434 gravity computation did not completely remove the edge effects or possible local wavelength
435 features of the Indian Hill fault. For example, the different polynomial trends applied to estimate
436 the regional trend for the San Gabriel and Chino, and San Bernardino basin might create sharp
437 discontinuities in the residual gravity map. Two further steps were taken to ensure inversion of
438 the time-to-basement in this area. Instead of taking the SG4 line as the edge of the San Gabriel
439 basin, we used it as a blending tool for both residual calculations by extending a few kilometers
440 eastward or westward, respectively for each basin (Figure 2b, c). In essence, this ensured the
441 SG4 line had similar residual Bouguer gravity values from two different regional trends
442 subtraction. We then purposely reinterpreted the SG4 time-to-basement to ensure a shallower
443 interpretation of the predicted time, as similar as possible to the actual RF times. The predicted
444 time constrained by gravity follows closely the established RF times in the north but with a
445 distinction of shorter times in the south. When evaluating this depth profile, the northern end is
446 better resolved than the southern end.

447 The Chino basin is deeper in the west and shallower in the east. A shallower north-south
448 trending segment is present east of SB4 and is likely attributed to the exposed bedrocks of the
449 Jurupa Hills in the south. The two deeper pockets, which are also highlighted by gravity lows, are
450 near the city of Upland and Chino. The basin shallows to 1 km towards the SB3 and SB5 lines.
451 The basin depth map has very shallow depths south of SB5 where the Jurupa Hills are located.
452 Slightly southwest of this, we find the Jurupa Valley which our model depicts as a deeper region
453 as shown in the SB3 line. While the basin topography in the center of the Chino basin does not
454 allow outright unequivocal interpretations, borehole data corroborated the deeper trend toward
455 the west (Wildermuth et al., 2005). The Wildermuth et al. (2005) report describes a series of
456 boreholes that penetrate crystalline bedrock in the east and sedimentary bedrock in the west at
457 similar drilling depths, suggesting a deeper west. The shallower eastern side relative to the deeper
458 western part of the Chino basin in the model reflects the shallower crystalline basement captured
459 in the boreholes.

460 The estimated basement shape of the San Bernardino basin suggests a pull-apart basin
461 structure described by extension along major fault zones. The strand of the San Jacinto fault
462 running through the San Bernardino basin is called the Claremont strand. There is ~2 km
463 subsidence associated with this strand of the SJF. The choice for the sediment-basement
464 interface favors a shallower interpretation for the SB6 line, which follows Ghose et al. (2022) and
465 is consistent with the intersection with SB2. This diverges from Wang et al. (2021) results, which
466 Ghose et al. (2022) interpret as an intra-crustal layer. The different interpretations of the sediment-
467 basement interface for SB2 between Ghose et al. (2022) and Wang et al. (2021) is the northern
468 segment; with Ghose et al. (2022) favoring a deeper structure while Wang et al. (2021) show a
469 thinner sedimentary layer of more uniform thickness. The gravity profile resembles the flat
470 structure of Wang et al. (2021), but it should be noted that the velocity model (Figure 6d) reveals
471 a low-velocity zone near Ghose et al. (2022) zone of subsidence. The depth profile constrains the

472 northern segment to a shallower depth than the southern segment which is bounded by the
473 Claremont strand. A possible reason for the discrepancy might be due to the exposed bedrock to
474 the northwest of the SB2 line. The regional trend removed the effects of the San Bernardino
475 Mountains, but it is possible that the effects from the exposed bedrock within the basin were not
476 well resolved.

477 **5 Conclusion**

478 The 3-D shape and depths of the northern Los Angeles basins were computed by
479 integrating seismic and Bouguer gravity measurements along with the surface and borehole
480 geology. Due to the densely spaced constraints along 10 individual seismic lines, this approach
481 was effective at determining the detailed geometry of the sediment-basement interface in an ~90-
482 km wide region extending from the southern SAF to downtown Los Angeles. Model validation
483 against 17 borehole recorded basement depths allowed us to address non-uniqueness and trade-
484 offs between seismic velocities and travel times. Gravity measurements constrained the 3-D
485 shape of the sediment-basement interface and delineated the effects of faults around the basins.
486 The basement shape and depths further contributed to improving a 3-D basin-scale velocity model
487 as a prior (Li et al., 2022). The triangular-shaped San Gabriel basin is a fault-bounded basin with
488 a maximum depth of 4.5 km in its western and easternmost centers. The Chino basin is broader
489 and substantially shallower than the San Gabriel basin and dominated by a 1.5-2 km thick
490 sedimentary layer in its western segment. The San Bernardino basin exhibits ~2 km subsidence
491 along the Claremont strand of the SJF, consistent with a pull-apart structure. Further work on
492 ground motion simulations is needed to evaluate the seismic hazard and risk of the northern Los
493 Angeles basins and improve ground shaking models for large earthquake ruptures such as the
494 forecasted M_w 7.8 on the southern San Andreas fault.

495

496 **Acknowledgments**

497 We are grateful to the hundreds of nodal deployment volunteers, Los Angeles residents, and
 498 business owners who hosted our instruments. We thank Liu et al. (2018), Wang et al. (2021), and
 499 Ghose et al. (2022) for providing their receiver function results. This research was supported by
 500 the National Science Foundation awards 2105358 and 2105320. The BASIN project was partly
 501 supported by U.S. Geological Survey awards GS17AP00002 and G19AP00015, and Southern
 502 California Earthquake Center awards 18029 and 19033. Data collection was supported by
 503 Louisiana State University and California Institute of Technology. Nodal instruments were
 504 provided by Incorporated Research Institutions for Seismology (IRIS), Portable Array Seismic
 505 Studies of the Continental Lithosphere (PASSCAL), University of Utah, Louisiana State
 506 University, and the University of Oklahoma.

507
 508

509 **Data Availability Statement**

510 The basement time was obtained from Liu et al. (2018), Wang et al. (2021), and Ghose et al.
 511 (2022). Li et al. (2022) provided the shear-wave velocity model. The basement depths obtained
 512 from well logs are publicly available through the Geologic Energy Management Division's
 513 (CalGEM) online mapping application Well Finder
 514 <https://www.conservation.ca.gov/calgem/Pages/WellFinder.aspx> and Buwalda (1940). The
 515 Bouguer gravity data was provided by the Pan American Center Earth and Environmental
 516 Science portal. Figures were plotted using the GMT software, PyGMT, and cartopy (Met Office,
 517 2010; Uieda et al., 2022; Wessel et al., 2019). The 3D basin depth model is available at
 518 <http://doi.org/10.22002/D1.20252>.

519
 520

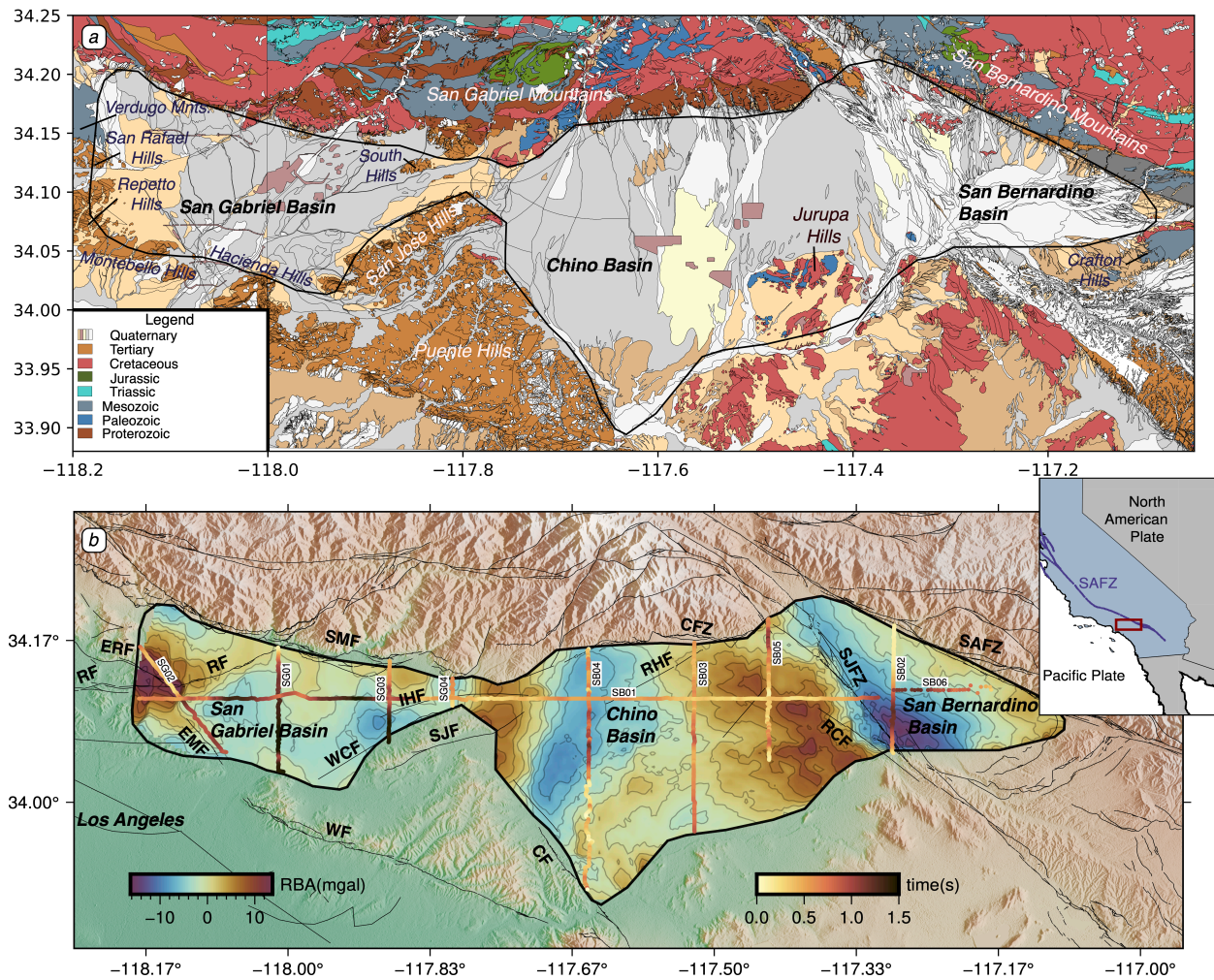
520 **References**

- 521 Anderson, M., Matti, J., & Jachens, R. (2004). Structural model of the San Bernardino basin,
 522 California, from analysis of gravity, aeromagnetic, and seismicity data: STRUCTURE OF
 523 THE SAN BERNARDINO BASIN. *Journal of Geophysical Research: Solid Earth*,
 524 109(B4). <https://doi.org/10.1029/2003JB002544>
- 525 Blomquist, W. (2021). The Natural Physical System of Chino Basin. In W. Blomquist, *The*
 526 *Realities of Adaptive Groundwater Management* (Vol. 27, pp. 13–21). Springer
 527 International Publishing. https://doi.org/10.1007/978-3-030-63723-1_2
- 528 Brocher, T. M. (2005). Empirical Relations between Elastic Wavespeeds and Density in the
 529 Earth's Crust. *Bulletin of the Seismological Society of America*, 95(6), 2081–2092.
 530 <https://doi.org/10.1785/0120050077>
- 531 Buwalda, J. P. (1940). *Geology of the Raymond Basin* (pp. 1–131). California Institute of
 532 Technology. <http://doi.org/10.22002/D1.20258>
- 533 Catchings, R. D., Rymer, M. J., Goldman, M. R., Gandhok, G., & Steedman, C. E. (2008).
 534 *Structure of the San Bernardino Basin along two seismic transects: Rialto-Colton Fault*
 535 *to the San Andreas Fault and along the I-215 Freeway (I-10 to SR30)* (Report No. 2008–
 536 1197; Version 1.0, Open-File Report). USGS Publications Warehouse.
 537 <https://doi.org/10.3133/ofr20081197>
- 538 Clayton, R., Persaud, P., Denolle, M., & Polet, J. (2019). Exposing Los Angeles's Shaky
 539 Geologic Underbelly. *Eos*, 100. <https://doi.org/10.1029/2019EO135099>
- 540 Denolle, M. A., Dunham, E. M., Prieto, G. A., & Beroza, G. C. (2014). Strong Ground Motion
 541 Prediction Using Virtual Earthquakes. *Science*, 343(6169), 399–403.
 542 <https://doi.org/10.1126/science.1245678>

- 543 Dolan, J. F., Gath, E. M., Grant, L. B., Legg, M., Lindvall, S., Mueller, K., Oskin, M., Ponti, D. F.,
544 Rubin, C. M., Rockwell, T. K., H, J., Treiman, A., Walls, C., & Yeats (compiler, R. S.
545 (n.d.). *1 Active Faults in the Los Angeles Metropolitan Region Southern California*
546 *Earthquake Center Group C**.
- 547 Dolan, J. F., Gath, E. M., Grant, L. B., Legg, M., Lindvall, S., Mueller, K., Oskin, M., Ponti, D. F.,
548 Rubin, C. M., Rockwell, T. K., Treiman, A., Walls, C., & Yeats, R. S. (2001). *Active*
549 *Faults in the Los Angeles Metropolitan Region* (SCEC Special Pub Southern California
550 Earthquake Center Group C; No. 001, p. 47). Southern California Earthquake Center.
551 <http://sceinfo.usc.edu/research/special/SCEC001activefaultsLA.pdf>
- 552 Dutcher, L. C., & Garrett, A. A. (1963). *Geologic and hydrologic features of the San Bernardino*
553 *area, California; with special reference to underflow across the San Jacinto fault.*
554 <https://doi.org/10.3133/wsp1419>
- 555 Florio, G. (2020). The Estimation of Depth to Basement Under Sedimentary Basins from Gravity
556 Data: Review of Approaches and the ITRESC Method, with an Application to the Yucca
557 Flat Basin (Nevada). *Surveys in Geophysics*, 41(5), 935–961.
558 <https://doi.org/10.1007/s10712-020-09601-9>
- 559 Frankel, A. (1993). Three-dimensional simulations of ground motions in the San Bernardino
560 Valley, California, for hypothetical earthquakes on the San Andreas fault. *Bulletin of the*
561 *Seismological Society of America*, 83(4), 1020–1041.
562 <https://doi.org/10.1785/BSSA0830041020>
- 563 Fuis, G. S., Ryberg, T., Godfrey, N. J., Okaya, D. A., & Murphy, J. M. (2001). Crustal structure
564 and tectonics from the Los Angeles basin to the Mojave Desert, southern California.
565 *Geology*, 29(1), 15–18. [https://doi.org/10.1130/0091-](https://doi.org/10.1130/0091-7613(2001)029<0015:CSATFT>2.0.CO;2)
566 [7613\(2001\)029<0015:CSATFT>2.0.CO;2](https://doi.org/10.1130/0091-7613(2001)029<0015:CSATFT>2.0.CO;2)
- 567 Ghose, R., Persaud, P., Wang, X., & Clayton, R. W. (2022). *High-frequency receiver function*
568 *profiles reveal sedimentary basin structure beneath the northern Los Angeles area* [In-
569 preparation].
- 570 Li, Y., Villa, V., Clayton, R., & Persaud, P. (2022). *Shear Wave Velocities in the San Gabriel and*
571 *San Bernardino Basins, California* (world). <https://doi.org/10.1002/essoar.10512118.1>
- 572 Liu, G., Persaud, P., & Clayton, R. W. (2018). Structure of the Northern Los Angeles Basins
573 Revealed in Teleseismic Receiver Functions from Short-Term Nodal Seismic Arrays.
574 *Seismological Research Letters*, 89(5), 1680–1689. <https://doi.org/10.1785/0220180071>
- 575 MacKevett, E. M. (1950). *The geology of the Jurupa Mountains, San Bernardino and Riverside*
576 *Counties, California* [Masters, California Institute of Technology].
577 <https://doi.org/10.7907/Y1V7-CG63>
- 578 Magistrale, H., Day, S. M., Clayton, R. W., & Graves, R. (2000). The SCEC Southern California
579 Reference Three-Dimensional Seismic Velocity Model Version 2. *Bulletin of the*
580 *Seismological Society of America*, 90(6B), S65–S76.
581 <https://doi.org/10.1785/0120000510>
- 582 Met Office. (2010). *Cartopy: A cartographic python library with a matplotlib interface.*
583 <http://scitools.org.uk/cartopy>
- 584 Morton, D. M., & Miller, F. K. (2006). *Geologic Map of the San Bernardino and Santa Ana 30' x*
585 *60' quadrangles, California* [Map]. <https://pubs.usgs.gov/of/2006/1217/>
- 586 Nourse, J. A. (2002). Middle Miocene reconstruction of the central and eastern San Gabriel
587 Mountains, southern California, with implications for evolution of the San Gabriel fault
588 and Los Angeles basin. In A. Barth, *Contributions to Crustal Evolution of the*
589 *Southwestern United States*. Geological Society of America. [https://doi.org/10.1130/0-](https://doi.org/10.1130/0-8137-2365-5.161)
590 [8137-2365-5.161](https://doi.org/10.1130/0-8137-2365-5.161)

- 591 Olsen, K. B., Day, S. M., Minster, J. B., Cui, Y., Chourasia, A., Faerman, M., Moore, R.,
592 Maechling, P., & Jordan, T. (2006). Strong shaking in Los Angeles expected from
593 southern San Andreas earthquake. *Geophysical Research Letters*, *33*(7).
594 <https://doi.org/10.1029/2005GL025472>
- 595 PACES. (2012). Pan-American Center for Earth and Environmental Studies.
596 <http://gis.utep.edu/paces/PACES%20Gravity%20Magnetics.htm>
- 597 Stephenson, W. J. (2002). Delineation of Faulting and Basin Geometry along a Seismic
598 Reflection Transect in Urbanized San Bernardino Valley, California. *Bulletin of the*
599 *Seismological Society of America*, *92*(6), 2504–2520.
600 <https://doi.org/10.1785/0120010222>
- 601 Tondi, R., Vuan, A., Borghi, A., & Argnani, A. (2019). Integrated crustal model beneath the Po
602 Plain (Northern Italy) from surface wave tomography and Bouguer gravity data.
603 *Tectonophysics*, *750*, 262–279. <https://doi.org/10.1016/j.tecto.2018.10.018>
- 604 Uieda, L., Tian, D., Leong, W. J., Jones, M., Schlitzer, W., Grund, M., Toney, L., Yao, J.,
605 Magen, Y., Materna, K., Newton, T., Anant, A., Ziebarth, M., Quinn, J., & Wessel, P.
606 (2022). *PyGMT: A Python interface for the Generic Mapping Tools (v0.7.0)*. Zenodo.
607 <https://doi.org/10.5281/zenodo.6702566>
- 608 Wang, X., Zhan, Z., Zhong, M., Persaud, P., & Clayton, R. W. (2021). Urban Basin Structure
609 Imaging Based on Dense Arrays and Bayesian Array-Based Coherent Receiver
610 Functions. *Journal of Geophysical Research: Solid Earth*, *126*(9).
611 <https://doi.org/10.1029/2021JB022279>
- 612 Weaver, K. D., & Dolan, J. F. (2000). Paleoseismology and Geomorphology of the Raymond
613 Fault, Los Angeles County, California. *Bulletin of the Seismological Society of America*,
614 *90*(6), 1409–1429. <https://doi.org/10.1785/0119990075>
- 615 Wessel, P., Luis, J. F., Uieda, L., Scharroo, R., Wobbe, F., Smith, W. H. F., & Tian, D. (2019).
616 The Generic Mapping Tools Version 6. *Geochemistry, Geophysics, Geosystems*, *20*(11),
617 5556–5564. <https://doi.org/10.1029/2019GC008515>
- 618 Wildermuth, M. J., LeClaire, J. P., Malone, A. E., Hwang, J. H., Rossi, J. V., & Atwater, R.
619 (2005). *Chino Basin Optimum Basin Management Program* (pp. 1–12).
620 [https://doi.org/10.1061/40763\(178\)140](https://doi.org/10.1061/40763(178)140)
- 621 Wright, T. L. (1991). *Chapter 3 Structural Geology and Tectonic Evolution of the Los Angeles*
622 *Basin, California*. <https://doi.org/10.1306/M52531C3>
- 623 Yeats, R. S. (2004). Tectonics of the San Gabriel Basin and surroundings, southern California.
624 *Geological Society of America Bulletin*, *116*(9), 1158. <https://doi.org/10.1130/B25346.1>
- 625 Yerkes, R. F., & Campbell, R. H. (2005). *Preliminary Geologic Map of the Los Angeles 30' x 60'*
626 *Quadrangle, Southern California* [Map]. U.S. Geological Survey.
627 <https://pubs.usgs.gov/of/2005/1019/>
628
629

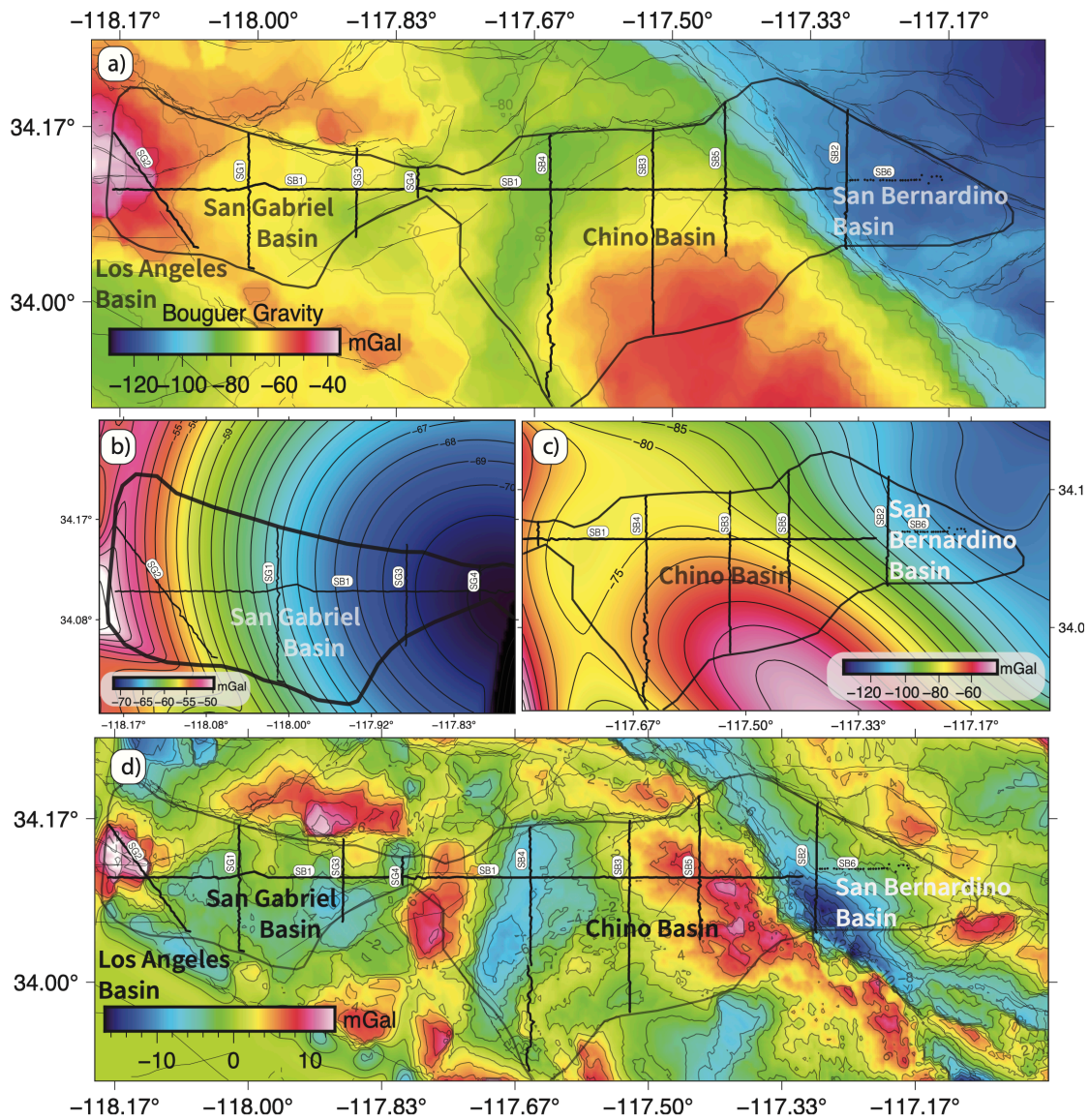
630 **Figures**



631

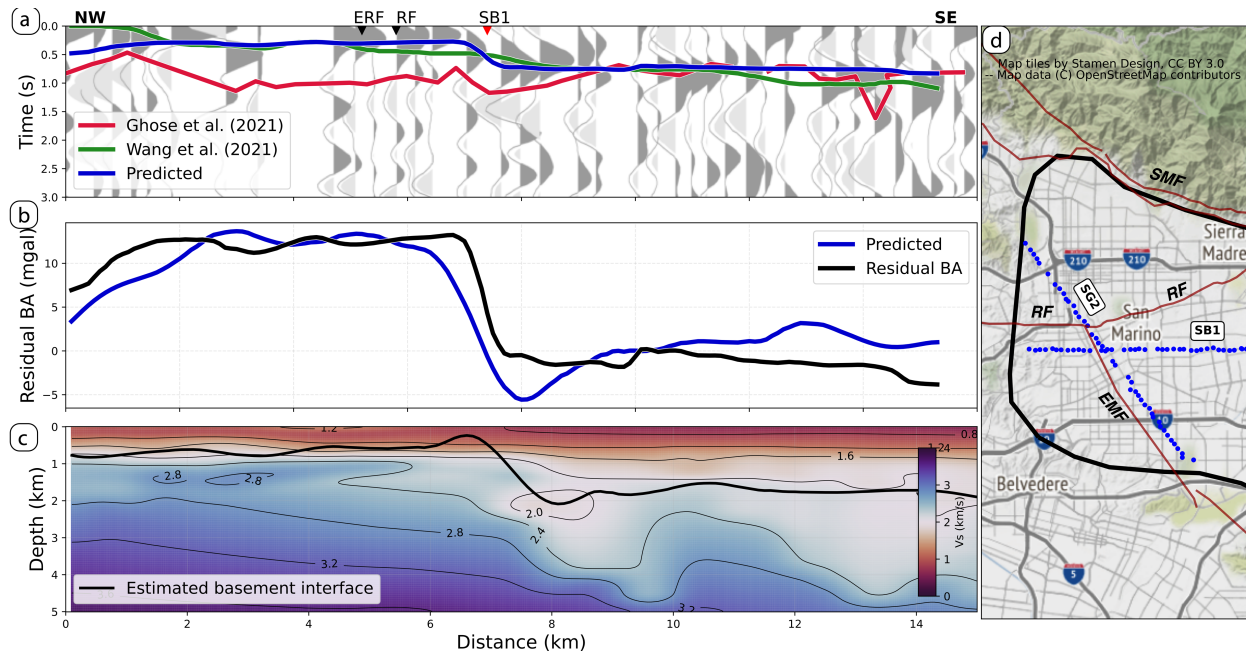
632 **Figure 1.** (a) Geologic map of the northern Los Angeles basins. The geologic age of the units is
 633 shown in the legend. Adapted from Yerkes and Campbell (2005) and Morton and Miller (2006).
 634 (b) Shaded-relief terrain map showing the outline of the BASIN survey. The contoured grid depicts
 635 the residual Bouguer gravity. Dark red-yellow-white circles show the time-to-basement in seconds
 636 along the 10 node lines. Black thin lines are fault locations. CF, Chino Hill Fault; CFZ, Cucamonga
 637 Fault Zone; EMF, East Montebello Fault; ERF, Eagle Rock Fault; IHF, Indian Hill Fault; RCF,
 638 Rialto Colton Fault; RF, Raymond Fault; RHF, Red Hill Fault; SJF, San Jose Fault; SJFZ, San
 639 Jacinto Fault Zone; SMF, Sierra Madre Fault; WCF, Walnut Creek Fault; WF, Whittier Fault;

640 SAFZ, San Andreas Fault Zone. The inset map outlines the study area concerning the transform
 641 plate boundary between the Pacific and North American plates.



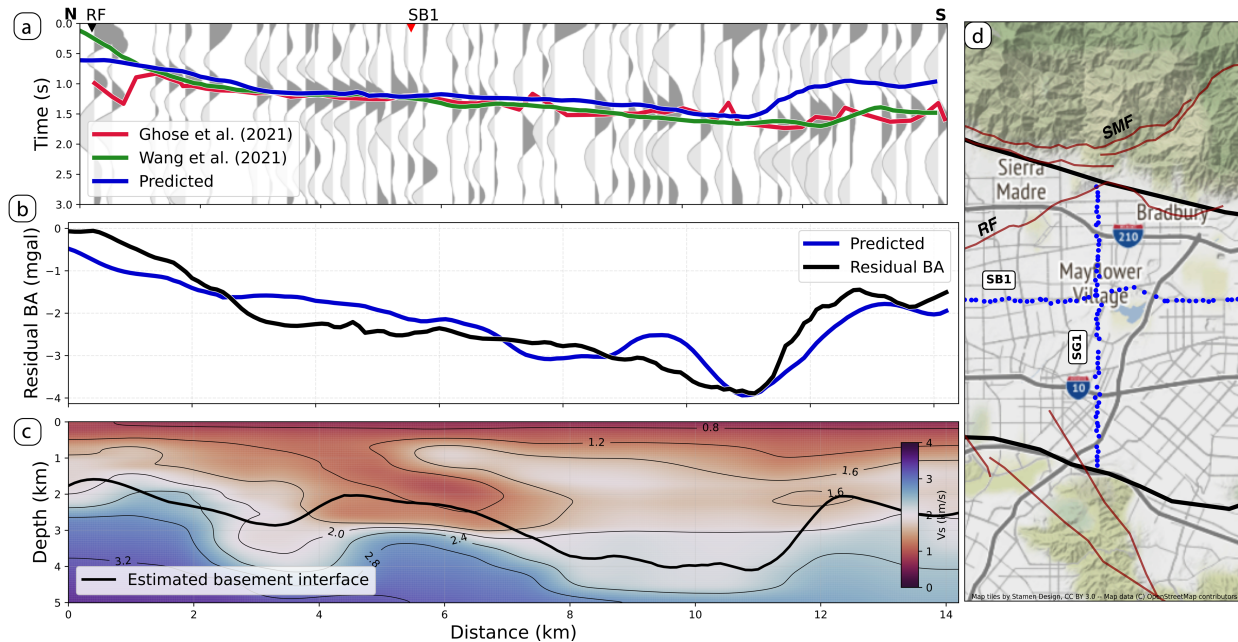
642 **Figure 2.** (a) Map of Bouguer gravity of the San Gabriel, Chino, and San Bernardino basins
 643 obtained from the PACES (2012) portal. (b) 2nd order polynomial trend for San Gabriel basin. (c)

644 7th order polynomial trend for Chino and San Bernardino basins. (d) Residual Bouguer anomaly
 645 map. The black outline shows the study area. Black lines represent the 10 nodal BASIN lines.



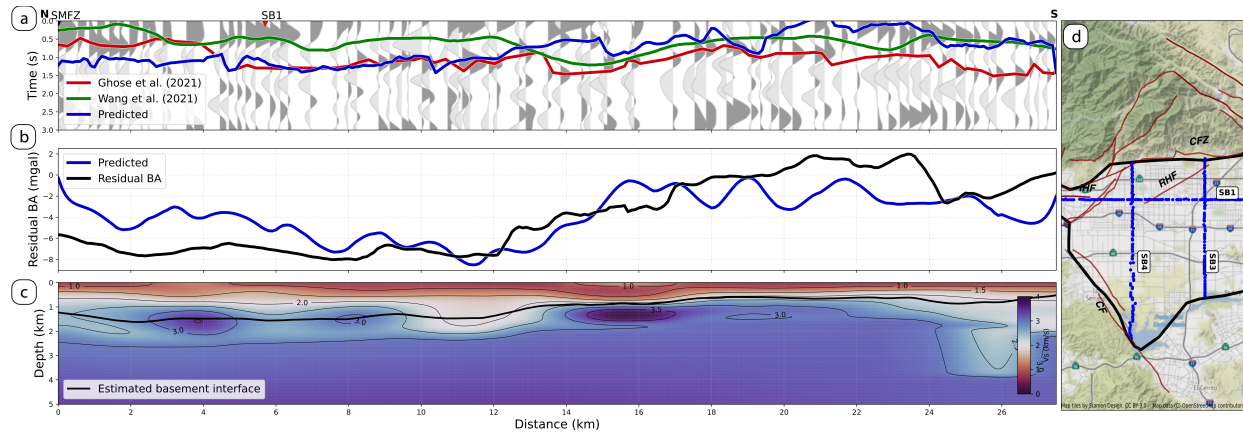
646

647 **Figure 3.** a) Profile along SG2 showing the time-to-basement from two RF studies and the
 648 predicted time-to-basement from this study. RF background from Ghose et al. (2022) is from a
 649 single event. b) Residual and predicted Bouguer anomaly is shown with black and blue lines,
 650 respectively. c) Shear wave velocity cross-section from Li et al. (2022) and the estimated
 651 basement surface determined by converting the blue line in a) to depth. d) Map showing the nodal
 652 stations of the SG2 line as blue dots. SB1 stations are included for reference. Maroon lines are
 653 fault locations. EMF, East Montebello fault; SMF, Sierra Madre fault; RF, Raymond fault.



654

655 **Figure 4.** a) Profile along SG1 showing the time-to-basement from two RF studies and the
 656 predicted time-to-basement from this study. RF background from Ghose et al. (2022) is from a
 657 single event. b) Residual and predicted Bouguer anomaly is shown with black and blue lines,
 658 respectively. c) Shear wave velocity cross-section from Li et al. (2022) and the estimated
 659 basement surface determined by converting the blue line in a) to depth. d) Map showing the nodal
 660 stations of the SG1 line as blue dots. SB1 stations are included for reference. Maroon lines are
 661 fault locations. SMF, Sierra Madre fault; RF, Raymond fault.

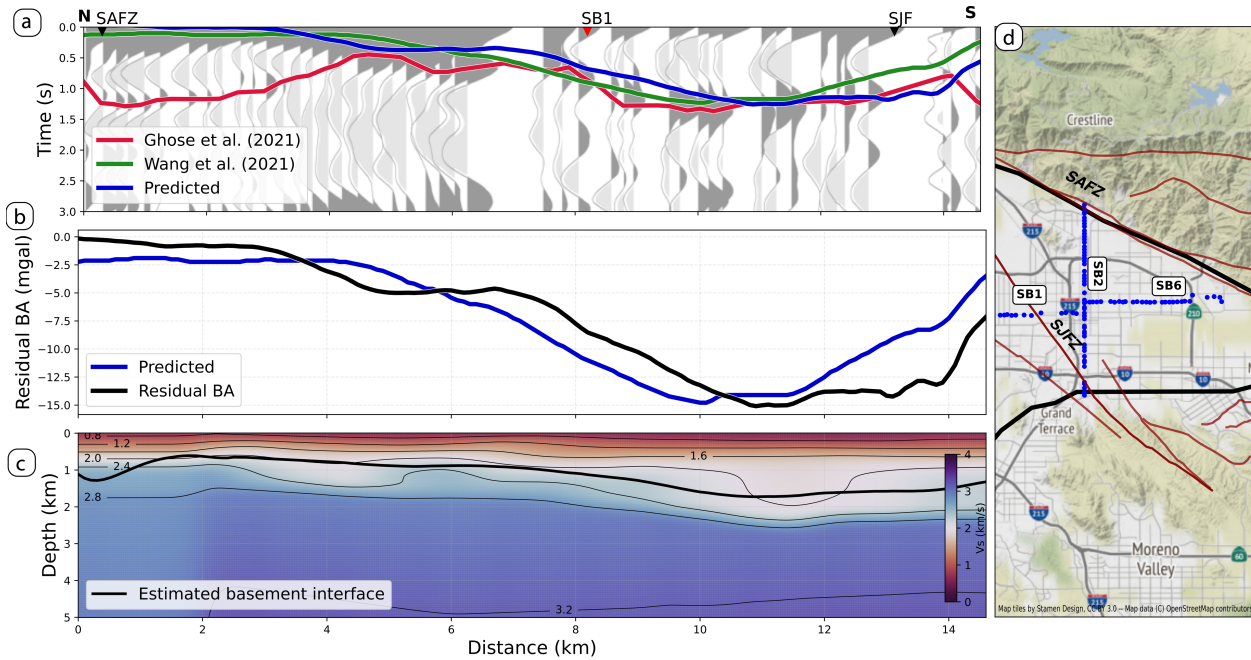


662

663 **Figure 5.** a) Profile along SB4 showing the time-to-basement from two RF studies and the
 664 predicted time-to-basement from this study. RF background from Ghose et al. (2022) is from a
 665 single event. b) Residual and predicted Bouguer anomaly is shown with black and blue lines,
 666 respectively. c) Shear wave velocity cross-section from Li et al. (2022) and the estimated
 667 basement surface determined by converting the blue line in a) to depth. d) Map showing the nodal
 668 stations of the SB4 line as blue dots. SB1 and SB3 stations are included for reference. Maroon

669 lines are fault locations. CF, Chino Fault; CFZ, Cucamonga Fault; IHF, Indian Hill Fault; RHF,
 670 Red Hill Fault.

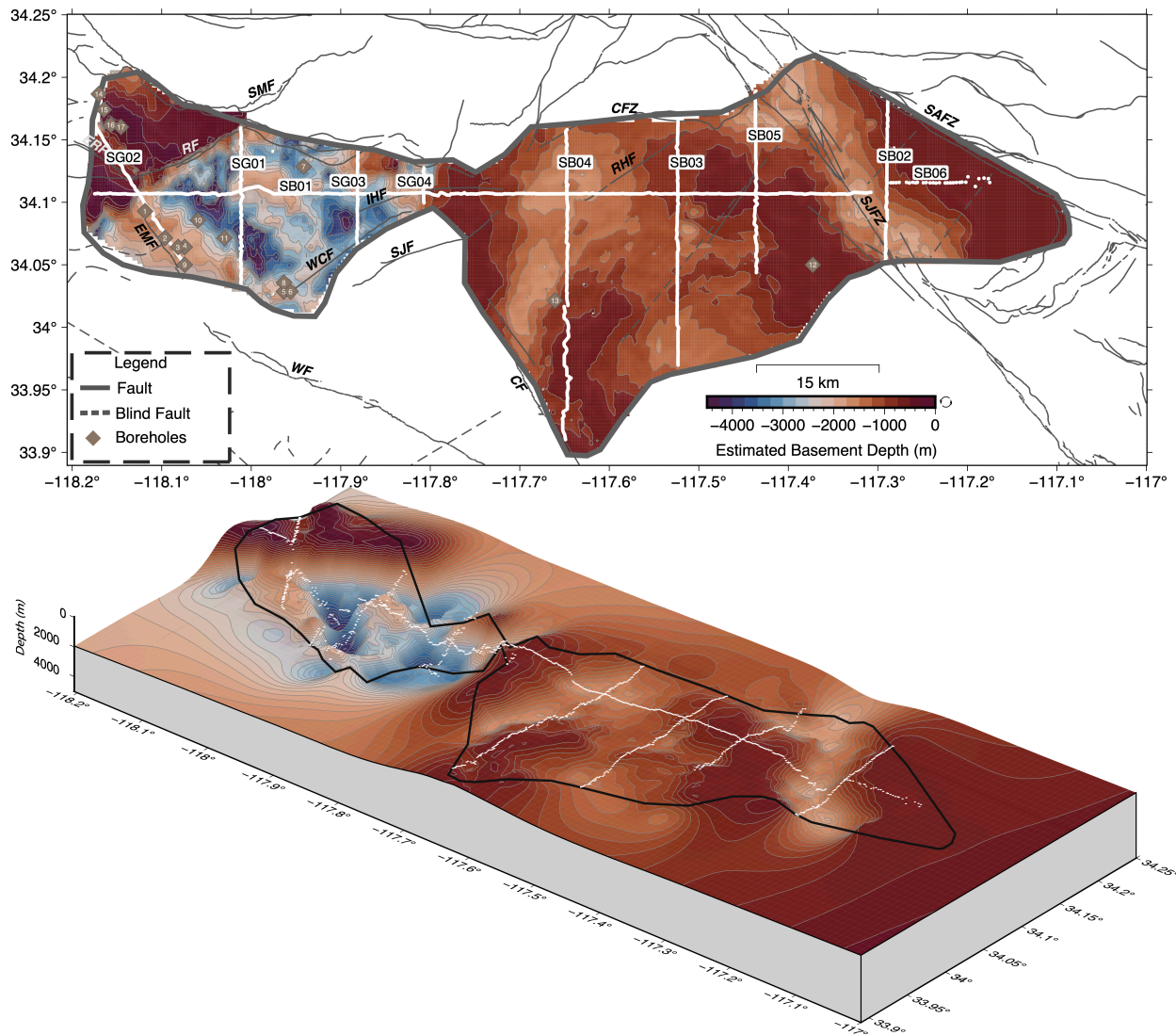
671



672

673 **Figure 6.** a) Profile along SB2 showing the time-to-basement from two RF studies and the
 674 predicted time-to-basement from this study. RF background from Ghose et al. (2022) is from a
 675 single event. b) Residual and predicted Bouguer anomaly is shown with black and blue lines,
 676 respectively. c) Shear wave velocity cross-section from Li et al. (2022) and the estimated
 677 basement surface determined by converting the blue line in a) to depth. d) Map showing the nodal

678 stations of the SB2 line as blue dots. SB1 and SB6 stations are included for reference. Maroon
 679 lines are fault locations. SAFZ, San Andreas Fault Zone; SJFZ, San Jacinto Fault Zone.



680
 681 **Figure 7.** a) Depth to basement map of the greater Los Angeles area's San Gabriel, Chino, and
 682 San Bernardino. The borehole numbers correspond to those listed in Table S1. b) Three-
 683 dimensional perspective view from the southeast of the basin depth map. Basement depths are
 684 unconstrained outside the region shown in a). The surface shows the depth in meters below sea
 685 level. Small white circles represent the 10 nodal lines of the BASIN survey. The dark gray line
 686 outlines the study area and encompasses the three basins. Solid black lines are faults and dashed
 687 black lines are blind faults. CF, Chino Hill Fault; CFZ, Cucamonga Fault Zone; EMF, East
 688 Montebello Fault; ERF, Eagle Rock Fault; IHF, Indian Hill Fault; RCF, Rialto Colton Fault; RF,
 689 Raymond Fault; RHF, Red Hill Fault; SAFZ, San Andreas Fault Zone; SJF, San Jose Fault; SJFZ,
 690 San Jacinto Fault Zone; SMF, Sierra Madre Fault; WCF, Walnut Creek Fault; WF, Whittier Fault.